aerospace

MDPI

Article

Flow Characteristics of Liquid Jet in Transverse Shear Crossflow

Chi Zhang [1], Yaguo Lyu [1,*], Le Jiang [1,2] and Zhenxia Liu [1]

[1] School of Power and Energy, Northwestern Polytechnical University, Xi'an 710072, China; zhangchi97@mail.nwpu.edu.cn (C.Z.); ljiang_nwpu@126.com (L.J.); zxliu@nwpu.edu.cn (Z.L.)
[2] AECC Sichuan Gas Turbine Establishment, Chengdu 610500, China
* Correspondence: yglu@nwpu.edu.cn; Tel.: +86-135-7210-7833

Abstract: The numerical simulation method was used to investigate the deflection and deformation process of a circular lubricating oil jet in transverse shear airflow. The numerical model was compared and validated against the experimental data. The physical parameters of Mobil jet Oil II were utilized in this simulation with the nozzle diameter ranging from 0.5 to 2.5 mm, the maximum liquid/gas momentum ratios varying from 10.35 to 165.50, and the injection angle ranging from 0 to 30° in the opposite airflow direction. The results show that an increase in the nozzle diameter decreases the degree of jet deflection. The higher airflow velocity causes more fluctuations in the oil-jet trajectory, while the higher oil-injection velocity reduces fluctuations in the trajectory. The parabolic curve equations were used to derive the trajectory equations for the jet column's pre-disintegration under both vertical incidence and a small angle of reverse airflow. The nozzle diameter and maximum oil/air momentum ratio were used to obtain a formula for the trajectory curve of the lubricating oil. Additionally, a formula for fitting the trajectory curve of oil injected in the opposite airflow direction regarding the injection angle was developed.

Keywords: crossflow; injection angle; liquid trajectory; numerical simulation; two-phase flow

Citation: Zhang, C.; Lyu, Y.; Jiang, L.; Liu, Z. Flow Characteristics of Liquid Jet in Transverse Shear Crossflow. *Aerospace* **2024**, *11*, 76. https://doi.org/10.3390/aerospace11010076

Academic Editor: Taro Handa

Received: 30 September 2023
Revised: 12 December 2023
Accepted: 28 December 2023
Published: 13 January 2024

1. Introduction

The liquid-injection method is used to deliver lubricating oil in aero engines, especially in the under-race lubrication structure. Lubricating oil is injected into the oil collector and transmitted to the bearing inner ring through an internal channel. Under the influence of centrifugal force and pressure, oil flows into the bearing cavity through the hole in the inner ring. A continuous oil column is observed during the oil collection process of the oil collector [1] and the oil discharge process of the bearing inner ring hole [2]. The flow characteristics of the oil column have a significant impact on the lubricating and cooling effects within the bearings [3]. During the oil collection process, the rotation of the components induces non-uniform airflow within the bearing cavity. The oil column undergoes deflection, deformation, collision, branching, and fragmentation due to aerodynamic effects and surface tension [4]. These phenomena can lead to the accumulation of lubricating oil in the oil collector, ultimately diminishing the oil collection efficiency of the under-race lubrication structure [5].

Extensive research has been carried out on the collection of lubricating oil in the radial oil collector of under-race lubrication structures. Paloma [6] researched on the capability of a scoop system to capture and retain delivered oil. Prabhakar and Abakr [7] demonstrated that oil loss due to the centrifugal effect is influenced by the location of the oil jet impacting the inner surface of the blade. Korsukova and Morvan [8] studied the radial under-race lubrication structure and found that oil collection efficiency decreases significantly when the oil impinges on the outer surface profile near the blade tip but improves when it impacts the outer surface contour near the blade root. Ardashkin and Borisov [9] investigated various parameters affecting oil collection efficiency and discovered that the maximum oil collection efficiency occurs when the injection direction is opposite to the rotation direction

of the oil collection ring. Qin [10] proposed an under-race oil supply lubrication device that incorporates a radial oil collection ring. The tangential orientation of the inner surface of the oil-collecting blade aligns with the relative velocity direction of the lubricating oil, which reduces collision and splashing of the oil on the inner surface. In his doctoral thesis, Qin [11] noted that the higher the initial velocity of the lubricating oil entering the inner surface of the oil-receiving scoop, the less likely the oil jet is to choke out. The mentioned research exemplifies that the oil trajectory directly impacts oil collection efficiency. To comprehend the various factors affecting the oil collection efficiency of the radial oil collection structure, it is crucial to examine the flow characteristics of the lubricating oil jet in the non-uniform airflow within the bearing cavity under varying conditions.

Numerous studies have been conducted on the flow of liquid jets in uniform airflow. Chen [12] and Wu [13] observed that the process of jet fragmentation is primarily divided into two stages: the transformation from a liquid column to a liquid block or large droplet is referred to as the primary breakup, and the further fragmentation of the liquid block or large droplet into smaller droplets is known as the secondary breakup. Mazallon [14] studied the deformation and fragmentation of a transverse jet using the pulse shadow method at room temperature and pressure. The research results showed that, as the gas Weber number increased, the transverse jet underwent three forms: bag crushing, composite crushing, and shear crushing. Zhou [15] analyzed the evolution process of the jet surface waves at different disturbance frequencies and the coupling effect of the jet tip and liquid core on the overall spray field from overall structure, liquid ligament, and droplet formation. Singh [16] proposed an efficient cooling technique for a modern aero-engine afterburner liner based on the combination of jet impingement and film cooling based on jet impinging. In recent years, researchers have conducted some research on jet flow in transverse shear airflow. Becker [17,18] investigated the liquid mist mixing characteristics of a direct fuel jet injected into two layers of opposite rotating annular channels. Deng [19] investigated the flow of an inviscid liquid jet in a transverse jet under shear load. The results showed that the two-dimensional shear airflow has a velocity gradient in the jet direction, only changing the effect of transverse aerodynamic forces on the surface waves of the jet. The effect of gas and liquid Weber numbers on jet fragmentation is similar to that of non-uniform airflow. Kong [20,21] investigated jet fragmentation in two types of non-uniform airflow with positive and negative velocity gradients. The results showed that the local jet momentum ratio, the fragmentation mechanism, and the penetration depth changed due to the distributed aerodynamic force on the jet in non-uniform airflow.

The aforementioned research on the under-race lubrication structure indicates that the trajectory and flow state of the lubricating oil jet in the radial oil collector significantly impact its oil collection efficiency. However, there is a gap in research concerning the trajectory of lubricating oil in oil collectors. Correspondingly, the jet trajectory in transverse shear crossflow has not been thoroughly studied. Especially, there is a lack of research on the jet flow in transverse shear crossflow when the jet direction is opposite to the airflow direction. This article aims to investigate the flow characteristics and trajectory of lubricating oil in transverse shear crossflow during the radial oil collection process thanks to numerical simulations. Calculated results are used in order to establish empirical formulas for the oil trajectory regarding nozzle diameter, maximum oil/air momentum ratio, and injection angle.

2. Numerical Simulation Method

2.1. Geometry and Grid

The physical calculation model for the oil jet in transverse shear crossflow is based on a radial lubricating oil collector for large engines. The geometric model, as shown in Figure 1, has the airflow direction along the positive y-axis and the direction when the oil is vertically incident along the positive z-axis. The x-axis direction is determined with the right-hand rule.

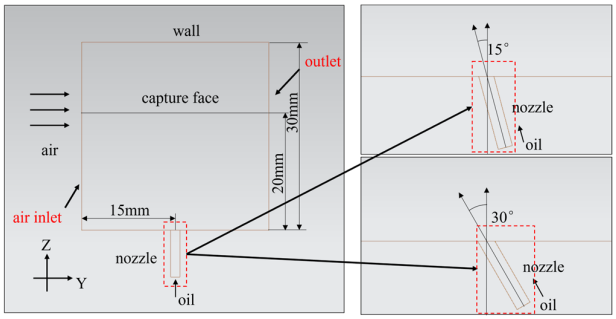

Figure 1. Geometric model.

The air inlet has dimensions of 30 mm × 18 mm, and the nozzle is positioned at the center of the bottom wall of the computational domain, maintaining a distance of 15 mm between the nozzle and the air inlet. The nozzle length is 7.5 mm. The injection angle is defined as the angle between the centerline of the oil inlet and the *z*-axis in the y–z plane. Oil is injected into the opposite direction of the crossflow. The red dash box area in the image indicates the oil inlet. The range of injection angles is determined with the angles that result in higher oil collection efficiency in the radial oil collector. The tip of the oil-collecting ring blade rotates to form a lubricating oil capture surface, and the corresponding capture surface in the crossflow is determined based on the tip surface. For reference, the distance between the blade tip and the nozzle of a specific oil collector is 20 mm. The capture surface in transverse shear crossflow is located at z = 20 mm.

The boundary conditions for the airflow in the oil collector include a set of stationary walls and rotating devices. To simplify the non-uniform airflow induced by the scoops in the radial oil-collecting ring, it is modeled as a linear transverse shear crossflow. The velocity distribution at the air inlet is represented as follows:

$$\begin{cases} v_g = V_{\max} & (z > h) \\ v_g = \frac{z}{h} V_{\max} & (z \le h) \end{cases} \quad (1)$$

The ranges of crossflow maximum velocity and oil injection velocity are determined based on the actual operating conditions of the oil collector. The pertinent parameter ranges are provided in Table 1. The density of the oil is 783.81 kg/m^3, and its viscosity is 0.001374 Pa·s. The density of air is 1.184 kg/m^3, and its viscosity is 0.00184 mPa·s. The surface tension of oil is 0.025 N/m.

Table 1. Related parameters affecting the trajectory of the lubricating oil center.

Related Parameter	Range
nozzle diameter, d	0.5~2.5 mm
crossflow maximum velocity, $V_{\max}$	40~120 m/s
oil injection velocity, V_j	10~25 m/s
maximum oil/air momentum ratio, $q_{\max}$	18.39~165.50
injection angle, θ	0~30°
Reynold number, Re_l	5705.6~28,528.1
Weber number, $\mathrm{We}_{g,\max}$	113.67~1022.98
Ohnesorge number, Oh	0.00621~0.01388
Froude number, Fr	22.56~56.41

Hexahedral structured grids are used to partition the overall computational domain. To ensure accurate flow in the boundary layer at the oil outlet, the boundary layer grid at the oil outlet is encrypted in Figure 2. Based on different working conditions, the height range of the first layer of different grids is calculated to be 2.745 × 10^{-3} mm to 7.180 × 10^{-3} mm, ensuring a y+ value less than 3. To minimize computational variations in the oil jets across different structures, the calculation domain, encompassing various nozzles, is meshed

using the same approach. The number of cells in different computational domains is standardized to approximately 9.5 million.

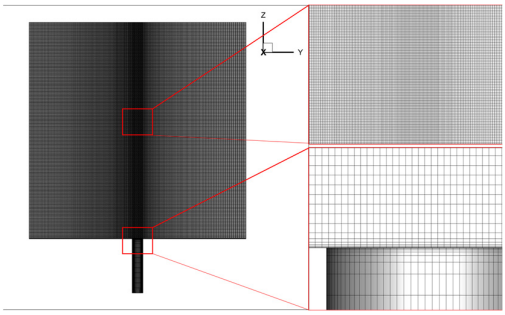

Figure 2. Grid refinement and division.

2.2. Boundary Condition and Calculation Methods

The oil inlet and air inlet are set as velocity inlet boundary conditions, and the outlet is set as pressure outlet boundary conditions. The given gauge pressure is 0 Pa (reference pressure is 1.013×10^{-5} Pa). All walls are designated as adiabatic wall boundary conditions without slip or penetration. The control equations in the numerical simulation calculations are discretized using the finite volume method. The time term is discretized using a first-order implicit format. Using center difference and PRESTO! (PREssure Staging Option) format discretizes the diffusion term and pressure term, respectively. Momentum, turbulent kinetic energy, and turbulent energy dissipation rate are discretized using a second-order upwind scheme.

Given that the Mach number of the air crossflow under the specified calculation conditions is less than 0.35, we assume that the airflow behaves as an incompressible fluid. The coupled implicit solver based on pressure was employed. Unsteady-state calculations were adopted, and the results are derived from the data obtained after the jet stabilized. Under the specified calculation conditions, the flow time scale ($t = d/V_j$) of the oil jet from the cylindrical nozzle ranges from 25 μs to 150 μs. The oil flow phenomenon in shear crossflow is an unsteady flow process. To minimize errors in the calculation of the oil center trajectory at a specific moment, a time interval of 20 μs has been employed, and the results of five oil trajectory calculations have been preserved. The lubricating oil center trajectory under a specific working condition is determined by averaging the calculations from five individual trajectories obtained under the same conditions.

2.3. Calculation Model

Due to the fact that the flow of a lubricating oil jet in non-uniform airflow involves a gas–liquid two-phase flow, the CLSVOF [22] method is used to capture the surface of the lubricating oil. The maximum Weber number of the oil jet ranges from 113.67 to 1022.98, and the maximum liquid/air pneumatic momentum ratio ranges from 18.39 to 165.50. The crushing mode of the jet is characterized by bag crushing and compound crushing. The oil column remains relatively intact within the computational domain. This article primarily investigates the flow state of the liquid column in the primary crushing mode. Therefore, atomization regimes are not considered. The realizable k-ε model, which is suitable for rotating flow, boundary layer flow with a strong reverse pressure gradient, flow separation, and secondary flow was used. Especially, it performs well when the curvature of the jet varies greatly. The results of this model are more accurate and reliable than the results obtained with the standard k-ε model. Within the velocity range of the oil jet, the Froude number of the oil jet is greater than 22.56, and the influence of the inertia force of the jet is much greater than that of its gravity.

The influence of gravity on the flow of lubricating oil can be ignored. Here is a set of two-phase flow control equations:

$$\frac{\partial \rho}{\partial t} + \nabla \bullet (\rho U) = 0 \tag{2}$$

$$\begin{cases} \frac{\partial(\rho w)}{\partial t} + \nabla \bullet (\rho w U) = -\frac{\partial p}{\partial x} + \frac{\partial \tau_{xx}}{\partial x} + \frac{\partial \tau_{yx}}{\partial y} + \frac{\partial \tau_{zx}}{\partial z} + \rho f_x \\ \frac{\partial(\rho u)}{\partial t} + \nabla \bullet (\rho u U) = -\frac{\partial p}{\partial y} + \frac{\partial \tau_{xy}}{\partial x} + \frac{\partial \tau_{yy}}{\partial y} + \frac{\partial \tau_{zy}}{\partial z} + \rho f_y \\ \frac{\partial(\rho v)}{\partial t} + \nabla \bullet (\rho v U) = -\frac{\partial p}{\partial z} + \frac{\partial \tau_{xz}}{\partial x} + \frac{\partial \tau_{yz}}{\partial y} + \frac{\partial \tau_{zz}}{\partial z} + \rho f_z \end{cases} \tag{3}$$

$$U = ui + vj + wk, \begin{cases} \rho f_x = \rho g - F_{sf,x} \\ \rho f_y = \rho g - F_{sf,y} \\ \rho f_z = \rho g - F_{sf,z} \end{cases} \tag{4}$$

f_x, f_y, and f_z are the volume force components in each direction. The treatment of the surface tension term draws inspiration from Brackbill's idea [23] of coupling surface tension as a volume force into the momentum equation. In the level-set method, the surface tension is given by Equation (7), while in the VOF method, the surface tension is given by Equation (10). The geometrical interface-front construction method is used here. The geometrical method involves a simple concept and is reliable in producing accurate geometrical data for the interface front. The values of the VOF and the level-set function are both used to reconstruct the interface front. Namely, the VOF model provides the size of the cut in the cell where the likely interface passes through, and the gradient of the level-set function determines the direction of the interface.

The phase function governing equation in the level-set method is given Equation (5). φ is the phase function in the level-set method.

$$\frac{\partial(\varphi)}{\partial t} + \nabla \bullet (\varphi U) = 0 \tag{5}$$

$$\varphi(x', t) = \begin{cases} +|d| & \text{if } x' \in \text{air phase} \\ 0 & \text{if } x' \in \Gamma \\ -|d| & \text{if } x' \in \text{oil phase} \end{cases} \tag{6}$$

$$F_{sf} = \frac{\overline{\rho}}{0.5(\rho_g + \rho_l)} \sigma \kappa \vec{n} \delta(\varphi) \tag{7}$$

$$\begin{cases} \overline{\rho} = (1 - F)\rho_g + F\rho_l \\ \overline{\mu} = (1 - F)\mu_g + F\mu_l \end{cases}, \vec{n} = \left. \frac{\nabla \varphi}{|\nabla \varphi|} \right|_{\varphi=0}, \kappa = \nabla \cdot \left. \frac{\nabla \varphi}{|\nabla \varphi|} \right|_{\varphi=0} \tag{8}$$

In the VOF method, α is the volume fraction of each fluid phase. When $\alpha = 0$, the cell is empty of the fluid. When $\alpha = 1$, the cell is full of the fluid. When $0 < \alpha < 1$, the cell contains the interface between the fluid and other fluids.

$$\frac{\partial(\alpha)}{\partial t} + \nabla \bullet (\alpha U) = 0 \tag{9}$$

$$F_{sf} = \sigma \kappa n \nabla \alpha \tag{10}$$

$$\vec{n} = \nabla \alpha_i, \kappa = \nabla \cdot \frac{\vec{n}}{\left| \vec{n} \right|} \tag{11}$$

The turbulent energy equation and dissipation equation of the Realizable k-ε turbulence model are given as follows:

$$\frac{\partial(\rho K)}{\partial t} + \frac{\partial(\rho \overline{u}_j K)}{\partial x_j} = \frac{\partial}{\partial x_j} \left[(\mu + \frac{\mu}{\mathrm{Pr}_K}) \frac{\partial K}{\partial x_j} \right] + P_K + G_b - \rho \varepsilon - Y_M \tag{12}$$

$$\frac{\partial(\rho \varepsilon)}{\partial t} + \frac{\partial(\rho \overline{u}_j \varepsilon)}{\partial x_j} = \frac{\partial}{\partial x_j} \left[(\mu + \frac{\mu_t}{\mathrm{Pr}_\varepsilon}) \frac{\partial \varepsilon}{\partial x_j} \right] + \rho C_1 \overline{S} \varepsilon - C_2 \rho \frac{\varepsilon^2}{K + \sqrt{v\varepsilon}} + C_{\varepsilon 1} \frac{\varepsilon}{k} C_{\varepsilon 3} G_b \tag{13}$$

where

$$C_1 = \max[0.43, \frac{\eta}{\eta+5}], \eta = S\frac{k}{\varepsilon}, S = \sqrt{2S_{ij}S_{ij}} \quad (14)$$

2.4. Numerical Method Verification

The commercial software Fluent 17.0 was employed for the simulation calculations. The verification calculation for the calculation method was conducted using the trial conditions proposed by Zhu as the boundary conditions [24]. The computational analysis involved water and air. The operating parameters were kept consistent with a water injection velocity of 3.8 m/s and an airflow velocity of 35.1 m/s.

The cross-section where the LS function is equal to 0 corresponds to the two-phase flow separation cross-section. The area where the LS function is greater than 0 represents the liquid volume. The calculated results are presented in Figure 3, where the black dots represent the liquid position when the LS phase function is greater than 0. The red line corresponds to the empirical formula proposed by Zhu et al., and the red dots represent the jet trajectory in Zhu's experiment. It can be observed that the deviation between the calculation results and the empirical formula is within 8.4%, while the simulation results align well with the observed jet trajectory. This suggests that the CLSVOF method can accurately capture the position of the lubricating oil.

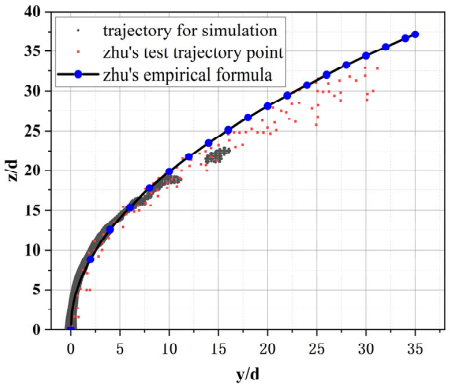

Figure 3. Comparison of water trajectory results with Zhu's experiments.

The oil jet is investigated under both uniform and transverse shear crossflow conditions. The injection velocity of the oil remains constant at 20 m/s. In the case of uniform airflow, the velocity is set at 120 m/s, while in the transverse shear crossflow field, the maximum velocity is also 120 m/s. Simulations of the lubricating oil jet were conducted in both scenarios, and the resulting jet trajectories are illustrated in Figure 4. It is evident that, due to the lower local airflow velocity, the deflection of the jet trajectory below a height of 8 mm is smaller than that of the oil trajectory in a uniform airflow. There is a notable difference in the oil trajectory between transverse shear and uniform airflow conditions.

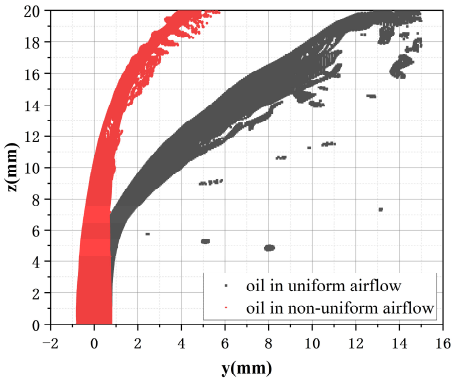

Figure 4. Comparison of oil trajectory in uniform and non-uniform airflow.

3. Results

3.1. Influence of Nozzle Diameter on Oil Jet Flow Characteristics

The oil injection velocity is 20 m/s, and the maximum crossflow velocity is 80 m/s with an injection angle of 0°. This study examines the impact of the nozzle diameter on the flow regime of the oil jet. As illustrated in Figure 5, the degree of oil trajectory deflection decreases with the increase in nozzle diameter. The center of the oil column on the capture surface advances as the nozzle diameter increases. With a constant injection velocity of oil and crossflow velocity distribution, the augmentation of the nozzle diameter results in a rapid increase in the mass flow rate of the lubricating oil, thereby weakening the acceleration effect of air on the lubricating oil. This observation is evident when comparing the oil volume fraction on the capture surface under various nozzle diameter conditions, as depicted in Figure 6. With an increase in the nozzle diameter, the shape of the oil column on the capture surface becomes more regular.

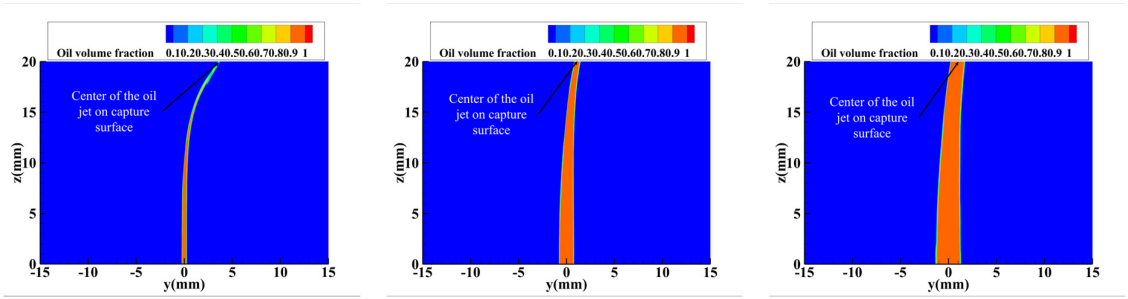

(**a**) d = 0.5 mm (**b**) d = 1.5 mm (**c**) d = 2.5 mm

Figure 5. Volume fraction of oil at the central plane under different nozzle diameters.

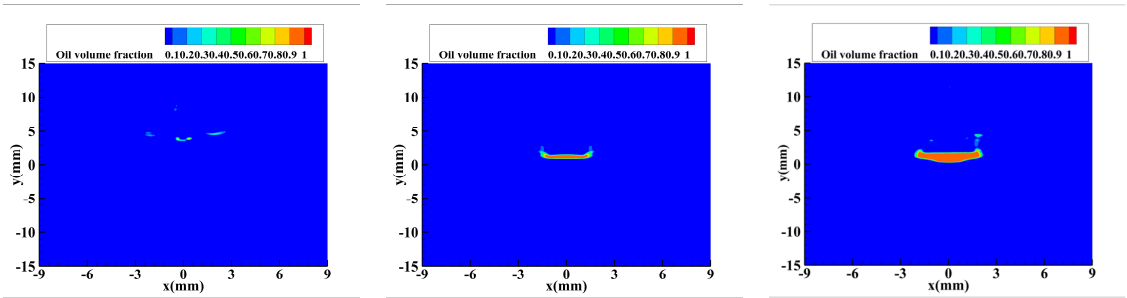

(**a**) d = 0.5 mm (**b**) d = 1.5 mm (**c**) d = 2.5 mm

Figure 6. Volume fraction of oil on the capture surface under different nozzle diameters.

The liquid film width of lubricating oil represents the length of the oil surface in the x-axis direction when the Level Set (LS) function equals 0 at z = h. Figure 7 illustrates the relationship between the liquid film width of lubricating oil on the capture surface and nozzle diameter. As the nozzle diameter increases, the liquid film width of the lubricating oil column also increases. When the nozzle diameter surpasses 2 mm, the change in the liquid film width of the oil column becomes less pronounced. Moreover, the ratio of liquid film width to nozzle diameter decreases with increasing nozzle diameter. This indicates that the influence of the nozzle diameter on the liquid film width of lubricating oil diminishes, and the liquid film width of oil approaches the nozzle diameter. This phenomenon indicates that the deformation of the oil jet liquid column in transverse shear crossflow decreases as the nozzle diameter increases. Subsequently, a diameter beyond 2 mm has little impact on the jet liquid column.

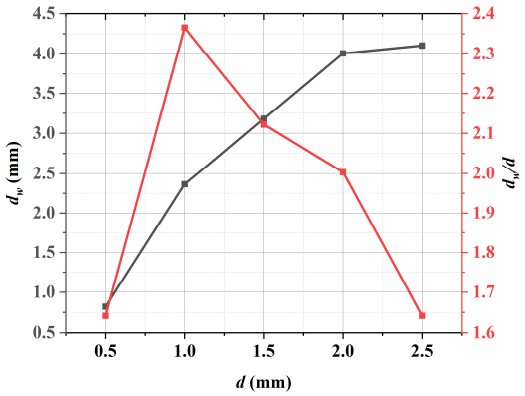

Figure 7. Variation in oil film width with nozzle diameter.

In the investigation of jet breakup in uniform airflow, researchers usually mark the upper boundary of the fluid in crossflow as a trajectory. However, the centerline trajectory of the oil column on the center plane can better reflect the displacement of the oil column and the position that the liquid column can reach on the capture surface. As shown in Figure 8, the distribution of center trajectories of lubricating oil with different diameters is given. At the same injection velocity and crossflow distribution, the center position of the oil on the capture surface is away from the vertical line of the nozzle center when the nozzle diameter is less than 1 mm. When the diameter increases from 1.5 mm to 2.5 mm, the change in the oil trajectory is relatively small. When the nozzle diameter is greater than 1.5 mm, increasing the nozzle diameter has little effect on the stability of the lubricating oil jet.

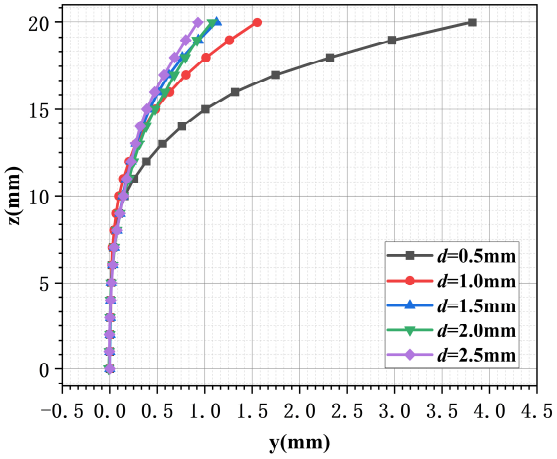

Figure 8. Oil center trajectory under different nozzle diameters.

3.2. Influence of Oil Injection Velocity on Oil Jet Flow Characteristics

The maximum velocity of the crossflow is 80 m/s, the nozzle diameter is 1.5 mm, and the injection angle is 0°. The injection velocity varies from 10 m/s to 25 m/s. As the injection velocity increases, the initial momentum of the lubricating oil column also increases. Figure 9 illustrates the distribution of lubricating oil on the center plane under three injection velocities. With the rising injection velocity, the initial momentum of the lubricating oil column increases, resulting in a shorter time for the oil to reach the same height. The acceleration effect of aerodynamic force weakens, and the deflection degree of the lubricating oil column decreases. When the injection velocity of the lubricating oil is less than 15 m/s, there is a significant disturbance in the lubricating oil column, and the position of the oil on the capture surface fluctuates considerably over time. As depicted in Figure 10, as the injection velocity of the oil increases, the shape of the oil on the capture surface regresses from a flat film shape to a meniscus shape, indicating a weakening influence of aerodynamic forces.

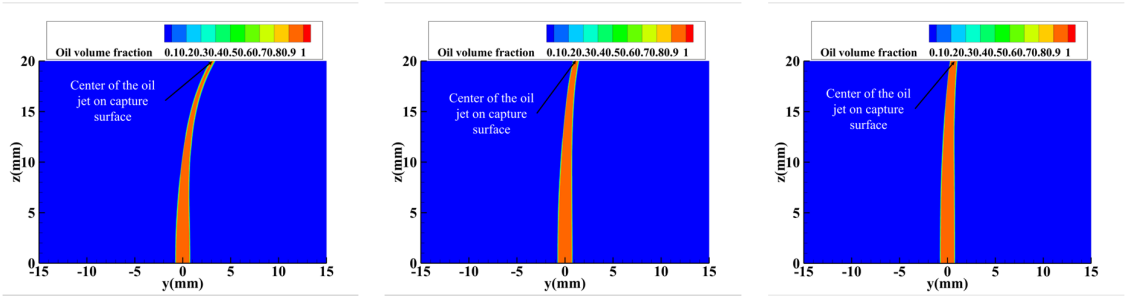

(**a**) V_j = 15 m/s (**b**) V_j = 20 m/s (**c**) V_j = 25 m/s

Figure 9. Volume fraction of oil at the central plane under different injection velocities.

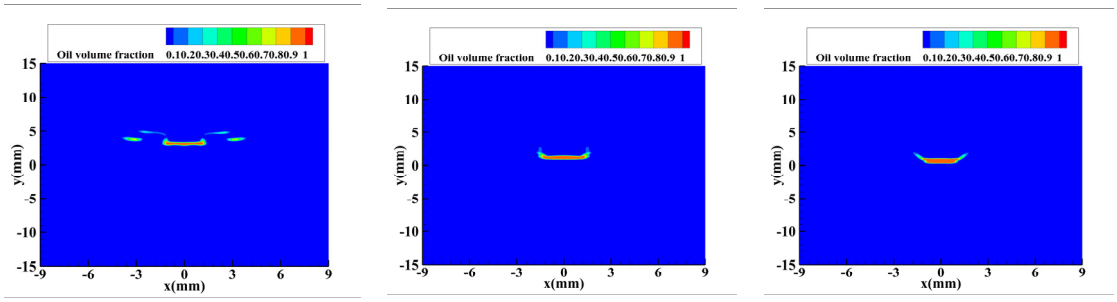

(**a**) V_j = 15 m/s (**b**) V_j = 20 m/s (**c**) V_j = 25 m/s

Figure 10. Volume fraction of oil on the capture surface under different injection velocities.

The change in the liquid film width with the injection velocity is depicted in Figure 11. It can be observed that, as the injection velocity of oil increases, the liquid film width of oil on the capture surface initially increases and then decreases. This occurs because the jet liquid column initially deforms along the direction of jet development, leading to an increase in the liquid film width. Subsequently, the liquid column breaks and peels off droplets due to the influence of Kelvin–Helmholtz (K-H) unstable waves, causing a decrease in the liquid film width of the oil column. However, the distribution distance of the oil droplets on the *x*-axis is increasing. This indicates that, when the lubricating oil flow rate increases to above 20 m/s, no obvious surface breakup occurs in the lubricating oil column below the capture surface.

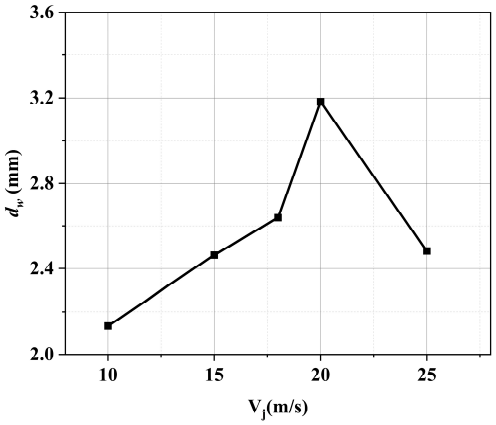

Figure 11. Variation in oil film width with injected velocity.

The oil center trajectories at different injection velocities are illustrated in Figure 12. When the injection speed of oil is less than 15 m/s, the oil column deflects significantly. Conversely, when the oil injection velocity exceeds 25 m/s, the change in the *y*-axis direction of the capture surface center trajectory does not exceed the nozzle radius.

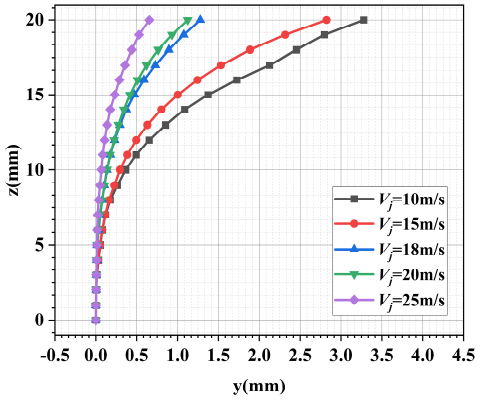

Figure 12. Oil center trajectory under different injection velocities.

3.3. Influence of Crossflow Velocity on Oil Jet Flow Characteristics

The oil injection velocity is 20 m/s, the nozzle diameter is 1.5 mm, and the injection angle is 0°. The maximum velocity of the crossflow varies from 40 m/s to 120 m/s. The maximum oil/air momentum ratio varies from 18.39 to 165.50. In linearly transverse shear crossflow, when the height (h) and the maximum velocity (V_{max}) of the crossflow are determined, the velocity distribution of the crossflow is also established. As depicted in Figure 13, the aerodynamic resistance in the crossflow increases, leading to an increase in the deflection of the lubricating oil column when the maximum velocity of the crossflow increases. When the maximum crossflow velocity is less than 80 m/s, the deflection of the lubricating oil column is minimal. However, under the working condition of a maximum crossflow velocity of 120 m/s, the disturbance of the tail surface of the lubricating oil column increases, and more surface peeling-off of the lubricating oil occurs. Similarly, statistical analysis was performed on the distribution of lubricating oil on the capture surface. Figure 14 shows that, when the maximum crossflow velocity is 40 m/s, the surface shape of the lubricating oil column exhibits a semi-lunar shape. As the crossflow velocity increases, the cross-section of the lubricating oil column on the capture surface is compressed and elongated, ultimately presenting a bag-like shape.

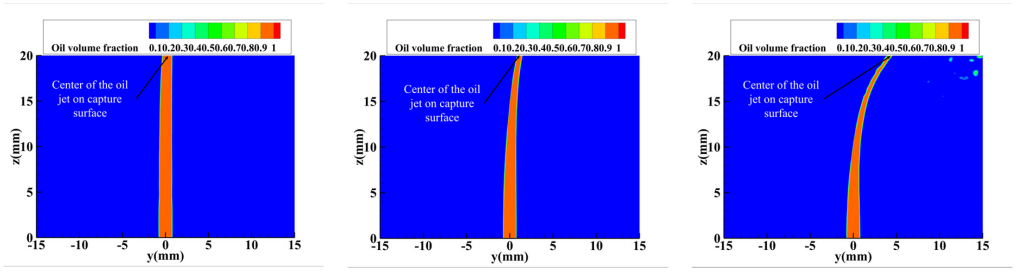

(**a**) V_{max} = 40 m/s (**b**) V_{max} = 80 m/s (**c**) V_{max} = 120 m/s

Figure 13. Volume fraction of oil on the central place under different crossflow velocities.

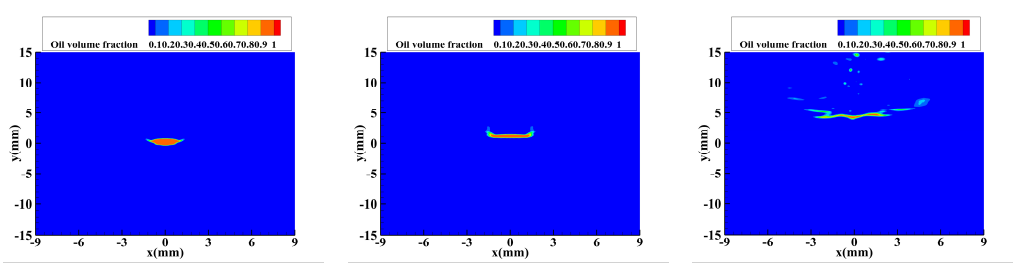

(**a**) V_{max} = 40 m/s (**b**) V_{max} = 80 m/s (**c**) V_{max} = 120 m/s

Figure 14. Volume fraction of oil on the capture surface under different crossflow velocities.

The relationship between the liquid film width of the oil column and the maximum crossflow velocity is depicted in Figure 15. The liquid film width of the oil column increases with the maximum velocity of the crossflow under the specified calculation conditions. When the maximum velocity of the crossflow surpasses 120 m/s, the oil column on the capture surface exhibits significant fluctuations, and the oil column is noticeably broken. However, it is important to note that the lubricating oil column will experience breakage, leading to a decrease in the liquid film width of the oil column when the crossflow velocity further increases.

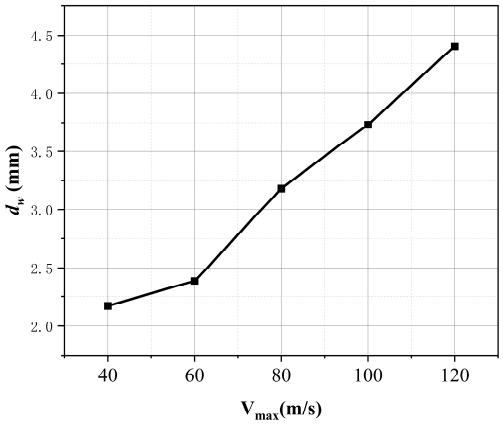

Figure 15. Variation in oil film width with different crossflow velocities.

The center trajectories of lubricating oil with different crossflow velocity distributions are shown in Figure 16. When the maximum velocity of the airflow is less than 60 m/s, the deflection of the oil column on the *y*-axis is less than the radius of the nozzle, and the jet experiences a bit of deflection. However, when the maximum velocity of the airflow exceeds 100 m/s, the deflection of the lubricating oil column on the capture surface on the *y*-axis increases rapidly.

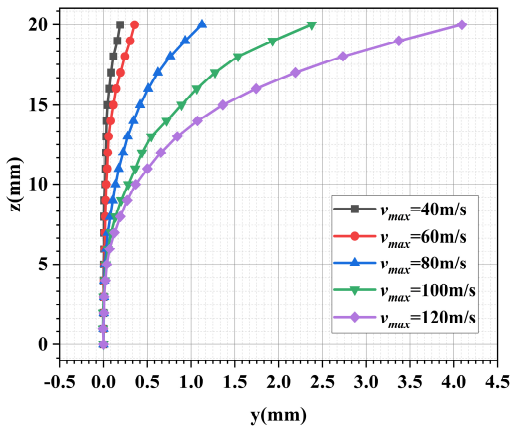

Figure 16. Oil center trajectory under different crossflow velocities.

The maximum oil/air momentum ratio is akin to the liquid/gas momentum ratio in a uniform crossflow. However, in a linear transverse shear crossflow, the maximum oil/air momentum ratio pertains to the highest momentum ratio under crossflow conditions. Figure 17 illustrates the center locus of oil under various maximum momentum ratio conditions. It is evident that, as the momentum ratio increases, the deflection of the oil column in the *y*-axis direction decreases.

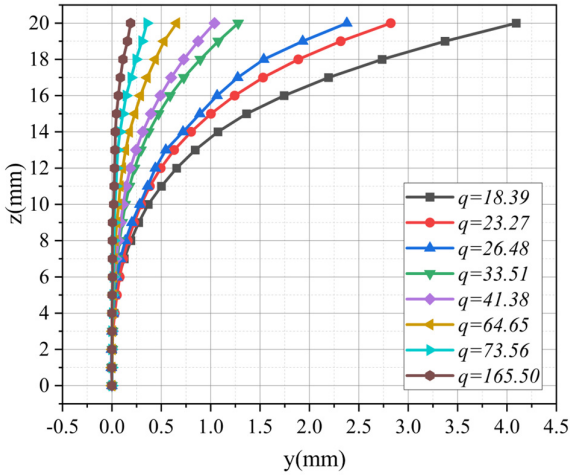

Figure 17. Oil center trajectory under different maximum oil/air momentum ratios.

3.4. Center Trajectory of Vertically Injected Lubricating Oil

The deflection of the oil column in the downstream direction of the jet is evidently attributed to aerodynamic drag. In this study, a phenomenon analysis approach is employed to establish simple correlations, avoiding the need to solve precise and complex control equations. The analysis focuses on balancing the liquid acceleration and air resistance in the crossflow direction to analyze the motion trajectory of the oil column. The force on the liquid column is shown in Figure 18. The deflection trajectory of lubricating oil in linear transverse shear crossflow is subsequently derived, building upon previous research [25].

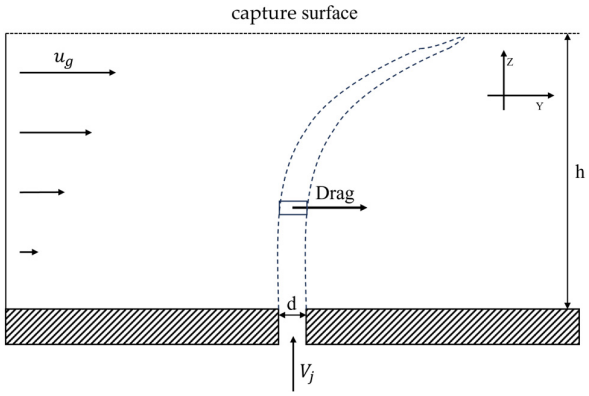

Figure 18. Sketch of the force diagram for the present phenomenological analysis.

We assume the liquid column can be modeled as a cylindrical micro-body with a nozzle outlet diameter (d) and length (l). Additionally, the diameter of the fluid elements is assumed to be constant. These assumptions neglect mass loss due to droplet breakage along the liquid column. For simplicity, the average resistance coefficient (C_D) is employed to account for the deformation and flattening of the liquid column. The origin of the y and z coordinates is set at the center of the nozzle outlet with y pointing downstream and z pointing in the direction of injection perpendicular to the wall. Given the small impact of gravity compared to aerodynamic forces, gravity is considered negligible. Furthermore, it is assumed that the z-direction velocity of the liquid column remains constant under the given calculation conditions. By introducing an average drag coefficient (C_D), the y-momentum equation can be expressed as follows:

$$\frac{\pi d^2 l \rho_l}{4}\left(\frac{\mathrm{d}u_l}{\mathrm{d}t}\right) = 0.5 C_D \rho_g (u_g - u_l)\left[(u_g - u_l)^2 + (v_g - v_l)^2\right]^{(1/2)} ld \tag{15}$$

The C_D represents the average resistance coefficient along the entire length of the liquid column in the airfield, encompassing the effects of liquid column deformation, flattening, droplet detachment, and disintegration. In the current calculation range, $(v_g - v_l)^2$ is estimated to be less than 25% of $(u_g - u_l)^2$ in most areas far from the nozzle and is ignored in the following derivation. In addition, u_l is estimated to be less than 16% of u_g. Therefore, we assume that the change in $u_g - u_l$ is also included in the C_D and can be represented by a constant. For subsonic airflow at low Mach numbers, ρ_g is a constant value. Due to $z = V_j t$ and $u_g = V_{\max}(z/h)$, Equation (15) can be integrated based on time, and the velocity component in the y-axis (u_l) is the following:

$$u_l = \frac{2C_D\rho_g V_{\max}^2 V_j^2}{3\pi\rho_l d h^2} t^3 \tag{16}$$

By integrating Equation (16), the axial position of the liquid column can be found:

$$\mathrm{y} = \frac{C_D\rho_g V_{\max}^2 V_j^2}{6\pi\rho_l d h^2} t^4 \tag{17}$$

Bring $z = V_j t$ in the formula, the trajectory equation is written as the following:

$$\frac{\mathrm{y}}{h} = \frac{C_D\rho_g V_{\max}^2 h}{6\pi\rho_l V_j^2 d} \left(\frac{z}{h}\right)^4 \tag{18}$$

From the derivation of Equation (18), we can observe that, in crossflow with linear velocity distribution, the trajectory equation of the jet is similar to the fluid trajectory equation in uniform crossflow, but Equation (18) separately addresses the influence of the nozzle diameter and combines it with the height of the crossflow to form a dimensionless number. The relationship between the y-coordinate of the lubricating oil and the momentum ratio, nozzle diameter, and z-coordinate can be expressed using a power function relationship. The nonlinear fitting of the center trajectory data under different operating conditions yields the formula for the center trajectory of the lubricating oil jet in the crossflow, as shown in Equation (19). The adjusted R-squared of the fitting formula and data is 0.9847.

$$\frac{y}{h} = 1.4919(q_{\max})^{-1.5215} \left(\frac{d}{h}\right)^{-0.9402} \left(\frac{z}{h}\right)^{3.7199} \tag{19}$$

As shown in Figure 19, the trajectory obtained from this fitting formula is compared to the center trajectory calculated on the central section. The results show that this fitting formula has a good goodness-of-fit with the oil trajectory.

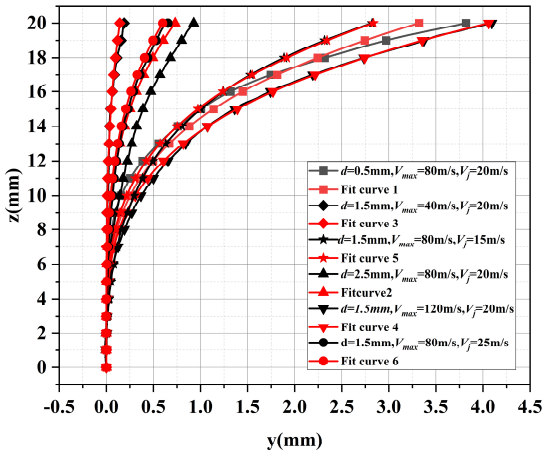

Figure 19. Comparison between the fitting curve and the center trajectory of the calculation example.

3.5. Influence of Oil Injection Angle on Oil Jet Flow Characteristics

The oil injection velocity is 20 m/s, the nozzle diameter is 1.5 mm, and the maximum velocity of the crossflow is 80 m/s. The injection angle varies from 0° to 30°. The injection angle of lubricating oil directly influences the initial velocity components of the oil jet in the y-axis and z-axis directions. With an increasing injection angle, the relative velocity of the lubricating oil to the crossflow in the y-axis direction rises, while the initial velocity component along the vertical crossflow direction decreases. The results are depicted in Figure 20. Within the calculation range, as the oil injection angle increases, the position of the oil on the capture surface gradually shifts from downstream of the nozzle to upstream of the nozzle. Figure 21 illustrates the distribution of oil on the capture surface at different injection angles. Across the injection angle range, the shape of the lubricating oil undergoes a transition from a liquid film shape to a crescent shape and then back to a liquid film shape. Notably, when the nozzle angle is between 10° and 20°, surface fragmentation occurs on both sides of the oil jet column.

The momentum equation in the y-axis direction for the trajectory equation of lubricating oil centers with different injection angles is the same as Equation (15). By integrating Equation (15) with the initial velocity of the liquid element in the y direction, u_l is obtained:

$$u_l = \frac{2C_D\rho_g V_{\max}^2 V_j^2}{3\pi\rho_l d h^2}\cos\theta^2 t^3 - V_j \sin\theta \tag{20}$$

By integrating Equation (20), the axial position of the oil column can be written as follows:

$$\mathrm{y} = \frac{C_D\rho_g V_{\max}^2 V_j^2 \cos\theta^2}{6\pi\rho_l d h^2} t^4 - V_j t \sin\theta \tag{21}$$

Bring $z = V_j t\cos\theta$ in the formula, the center trajectory equation of the lubricating oil is as follows:

$$\frac{\mathrm{y}}{h} = \left(\frac{C_D}{6\cos\theta^2\pi}\right)\left(\frac{\rho_g V_{\max}^2}{\rho_l V_j^2}\right)\left(\frac{d}{h}\right)^{-1}\left(\frac{z}{h}\right)^4 - \left(\frac{z}{h}\right)\tan\theta \tag{22}$$

The empirical Equation (23) formula for fitting the center trajectory of the lubricating oil with injection angle is finally obtained by fitting the relevant trajectory data in the form of a power function relationship inspired by Equation (22) formulation.

$$\frac{y}{h} = 1.4919(q_{\max})^{-1.5215}\left(\frac{d}{h}\right)^{-0.9402}\left(\frac{z}{h}\right)^{3.7199} - \left(\frac{z}{h}\right)\tan\theta \tag{23}$$

The Equation (23) fits the trajectory data with an R-squared equal to 0.9989.

To verify the reliability of the calculation results, a working condition different from the data used for fitting was selected. The chosen working conditions are an injection angle of 10°, nozzle diameter of 1.5 mm, injection velocity of 20 m/s, and maximum crossflow velocity of 80 m/s. The calculation results and fitting curve are illustrated in Figure 22. The black dots in the figure represent the oil column when the LS function is greater than 0, and the red line is the lubricant center trajectory drawn with the obtained fitting formula Equation (23). The trajectory calculated with the fitting formula in the figure aligns well with the distribution range of the lubricating oil, demonstrating a good correlation between the lubricating oil trajectory and the fitting curve.

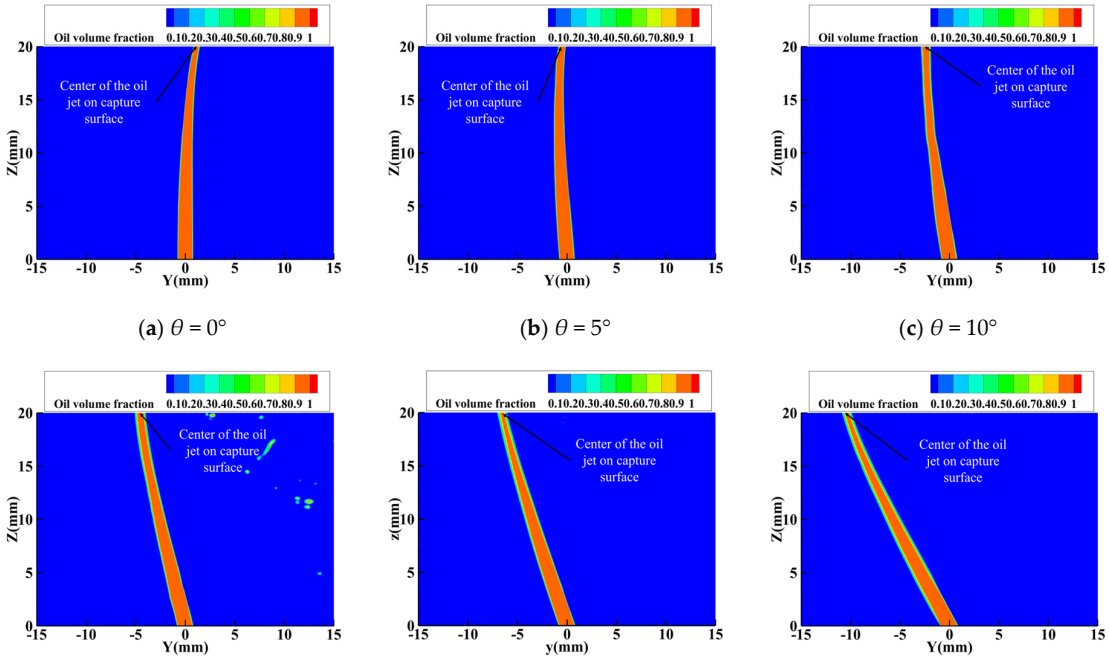

(**a**) $\theta = 0°$ (**b**) $\theta = 5°$ (**c**) $\theta = 10°$

(**d**) $\theta = 15°$ (**e**) $\theta = 20°$ (**f**) $\theta = 30°$

Figure 20. Volume fraction of oil on the central plane under different injection angles.

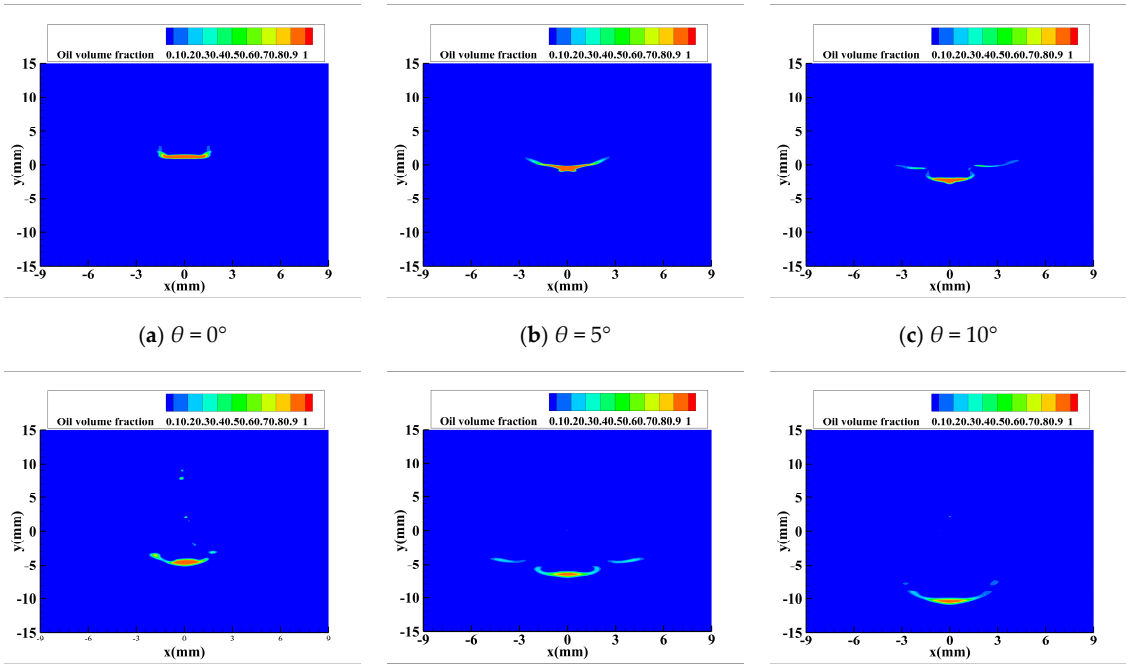

(**a**) $\theta = 0°$ (**b**) $\theta = 5°$ (**c**) $\theta = 10°$

(**d**) $\theta = 15°$ (**e**) $\theta = 20°$ (**f**) $\theta = 30°$

Figure 21. Volume fraction of oil on the capture surface under different injection angles.

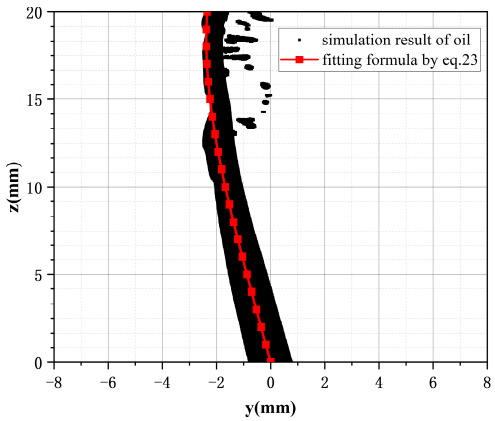

Figure 22. Comparison of lubricating oil distribution and fitting curve with Equation (23).

4. Discussion

This study employed precise, unsteady simulation methods to investigate the impact of injection angle, oil injection velocity, air velocity, and nozzle diameter on crossflow characteristics. The primary focus was on examining changes in oil trajectory under various parameter influences and the distribution of oil on the capture surface. The following conclusions were drawn:

1. As the nozzle diameter increases, the acceleration of the lubricating oil jet by aerodynamic forces becomes progressively challenging. Beyond a nozzle diameter of 2 mm, further increases have negligible effects on the jet trajectory. Moreover, with an elevation in the oil injection velocity, the deflection of the liquid column diminishes, leading to a more consistent distribution and diameter alterations of the oil on the capture surface. However, with an augmentation in the maximum crossflow velocity, the deflection degree of the lubricating oil column amplifies, and the fragmentation pattern intensifies, resulting in a more irregular oil distribution on the collection surface.
2. The trajectory equation for the oil jet in transverse shear crossflow was derived by employing the forces acting on a simplified micro-elemental body. The associated parameters were then fitted using a power function, yielding the fitting equation for the oil center trajectory under vertical injection conditions. The trajectory equation of the oil jet under the condition of injection in the opposite airflow direction was analyzed using the same method and subsequently simplified. All jet data were fitted using a power function, resulting in the fitting formula for the lubricating oil center trajectory at a small angle against the airflow direction.
3. Researchers can employ the jet trajectory fitting formula to ascertain the primary trajectory of the jet within the radial ring lubrication structure under engine operating conditions. This information can be utilized to design the internal surface structure of radial oil collection blades, thereby enhancing oil collection efficiency.

Author Contributions: Conceptualization, C.Z. and L.J.; methodology, C.Z.; software, C.Z.; validation, C.Z., Y.L. and Z.L.; formal analysis, C.Z.; investigation, C.Z. and L.J.; resources, C.Z.; data curation, C.Z.; writing—original draft preparation, C.Z.; writing—review and editing, C.Z. and Z.L.; visualization, C.Z. and L.J.; supervision, C.Z. and L.J.; project administration, C.Z.; funding acquisition, Y.L. All authors have read and agreed to the published version of the manuscript.

Funding: This research was funded by National Science and Technology Major Project under Grant No. J2019-III-0023-0067.

Data Availability Statement: Data are available through the corresponding author.

Conflicts of Interest: Author Le Jiang was employed by the company AECC Sichuan Gas Turbine Establishment. The remaining authors declare that the research was conducted in the absence of any commercial or financial relationships that could be construed as a potential conflict of interest.

Nomenclature

C_D	drag coefficient	$V_{\max}$	maximum cross airflow velocity
d	nozzle diameter	x	the spanwise direction of the oil column
d_w	oil film extension width	y	transverse shear crossflow direction
h	height of transverse shear crossflow	z	vertical bottom wall direction
i	unit vector in the y-axis direction	θ	nozzle injection angle
j	unit vector in the z-axis direction	ρ	density
k	unit vector in the x-axis direction	σ	surface tension coefficient
p	pressure	μ	viscosity
q	liquid/gas momentum ratio, $q = \rho_l V_l^2 / \rho_g V_g^2$		
$q_{\max}$	maximum liquid/gas momentum ratio, $q_{\max} = \rho_l V_l^2 / \rho_g V_{\max}^2$		
t	time	Re_l	Reynolds number. $\mathrm{Re}_l = \rho_l V_j^2 d / \sigma$.
u	the velocity component on the y-axis	$\mathrm{We}_{\mathrm{g,max}}$	Weber number. $\mathrm{We}_{\mathrm{g,max}} = \rho_g {V_{\max}}^2 d / \sigma$
v	the velocity component on the z-axis	Oh	Ohnesorge number. $Oh = \mu / \sqrt{\rho_l \sigma d}$.
w	the velocity component on the x-axis	Fr	Froude number. $Fr = V_j / \sqrt{gh}$.
V_j	lubricating oil injection velocity	F_{sf}	surface tension
Subscripts			
g		gas	
l		liquid	
max		maximum	

References

1. Jiang, L.; Liu, Z.; Lyu, Y. Internal Flow Field Analysis and Optimization Structure of Oil Scoop Blade in Under-Race Lubrication Structure. *J. Propuls. Technol.* **2022**, *43*, 200251.
2. Liu, Z.; Xu, R. Analysis of the Phenomenon of Non-Cylindrical Liquid Flow Falling Off in Transverse Air Flow in Under-Race Lubrication. *Lubr. Eng.* **2021**, *46*, 136–140. [CrossRef]
3. Bao, H.; Hou, X.; Lu, F. Analysis of Oil-Air Two-Phase Flow Characteristics inside a Ball Bearing with Under-Race Lubrication. *Processes* **2020**, *8*, 1223. [CrossRef]
4. Zhu, D.; Cheng, G. A 3D CFD simulation of oil spray-collection and delivery process in an aeroengine inter-shaft bearing. *Chin. J. Aeronaut.* **2022**, *35*, 366–378. [CrossRef]
5. Jiang, L.; Liu, Z.; Lyu, Y. Numerical Study on Flow Characteristics of Liquid Jet in Airflows. In Proceedings of the ASME Turbo Expo ASME Turbo Expo 2019: Turbomachinery Technical Conference and Exposition, Phoenix, AZ, USA, 17–21 June 2019; Volume 1. [CrossRef]
6. Cageao, P.P.; Simmons, K. Assessment of the Oil Scoop Capture Efficiency in High Speed Rotors. *J. Eng. Gas Turbines Power-Trans. ASME* **2019**, *141*, 012401. [CrossRef]
7. Prabhakar, A.; Abdalla Abakr, Y.; Simmons, K. Effect of Vortex Shedding on the Performance of Scoop Based Lubrication Devices. In Proceedings of the ASME Turbo Expo 2017: Turbomachinery Technical Conference and Exposition, Charlotte, NC, USA, 26–30 June 2017; Volume 7A. [CrossRef]
8. Korsukova, E.; Morvan, H. Computational Fluid Dynamics Study of Oil Behavior in a Scoop, and Factors Affecting Scoop Capture Efficiency. *J. Eng. Gas Turbines Power-Trans. ASME* **2020**, *142*, 051008. [CrossRef]
9. Ardashkin, I.; Borisov, E.A. Investigation of the influence of the speed and direction of the oil jet on the efficiency of the oil scoop operation in the oil supply system to the bearings of the gas turbine engine. *Aerosp. Eng.* **2017**, *4*, 16–25. [CrossRef]
10. Qin, J.W. Research on High Oil Capture Efficiency Under-Race Lubrication Technology of High Speed Bearing for Aeroengine. Ph.D. Thesis, Central South University, Changsha, China, 2022.
11. Qin, J.W.; Guo, H.; Zhou, L.; Cao, P. Oil Receiving Ring and Oil Supply Lubrication Device under the Ring. Chinese patent CN111878237B, 16 November 2021.
12. Chen, T.; Smith, C.; Schommer, D.; Nejad, A. Multi-zone behavior of transverse liquid jet in high-speed flow. In Proceedings of the 31st Aerospace Sciences Meeting, Reno, NV, USA, 11–14 January 1993; p. 453. [CrossRef]
13. Wu, P.K.; Kirkendall, K.A.; Fuller, R.P.; Nejad, A.S. Breakup processes of liquid jets in subsonic crossflows. *J. Propuls. Power* **1997**, *13*, 64–73. [CrossRef]
14. Mazallon, J.; Dai, Z.; Faeth, G. Aerodynamic primary breakup at the surface of nonturbulent round liquid jets in crossflow. In Proceedings of the 36th AIAA Aerospace Sciences Meeting and Exhibit, Reno, NV, USA, 12–15 January 1998; p. 716. [CrossRef]

15. Zhou, C.; Zou, J.; Zhang, Y. Effect of Streamwise Perturbation Frequency on Formation Mechanism of Ligament and Droplet in Liquid Circular Jet. *Aerospace* **2022**, *9*, 191. [CrossRef]
16. Singh, A.K.; Kumar, S.; Singh, K. Experimental and Numerical Study on the Combined Jet Impingement and Film Cooling of an Aero-Engine Afterburner Section. *Aerospace* **2023**, *10*, 589. [CrossRef]
17. Becker, J.; Hassa, C. Liquid fuel placement and mixing of generic aeroengine premix module at different operating conditions. *ASME J. Eng. Gas Turbines Power* **2003**, *125*, 901–908. [CrossRef]
18. Becker, J.; Heitz, D.; Hassa, C. Spray dispersion in a counter-swirling double-annular air flow at gas turbine conditions. *At. Sprays* **2004**, *14*, 15–36. [CrossRef]
19. Deng, T.; Li, J. Breakup mechanism of inviscid liquid transverse jet in shear airflow. *Acta Aeronaut. Astronaut. Sin.* **2021**, *42*, 124464. [CrossRef]
20. Kong, X.; He, W. Spray characteristics of liquid jet in nonuniform crossflow. *J. Aerosp. Power* **2022**, *37*, 534–544. [CrossRef]
21. Wang, K.; Kong, X. Investigation on trajectory and penetration of liquid jet in non-uniform velocity crossflow. *J. Aerosp. Power* **2023**, *38*, 1316–1327. [CrossRef]
22. Sussman, M.; Puckett, E.G. A coupled level set and volume-of-fluid method for computing 3D and axisymmetric incompressible two-phase flows. *J. Comput. Phys.* **2000**, *162*, 301–337. [CrossRef]
23. Brackbill, J.U.; Kothe, D.B.; Zemach, C. A continuum method for modeling surface tension. *J. Comput. Phys.* **1992**, *100*, 335–354. [CrossRef]
24. Zhu, Y.; Huang, Y. Experiment on the breakup of round liquid jets in cross airflows. *J. Aerosp. Power* **2010**, *25*, 2261–2266. [CrossRef]
25. Fuller, R.P.; Wu, P.K.; Kirkendall, K.A.; Nejad, A.S. Effects of injection angle on atomization of liquid jets in transverse airflow. *AIAA J.* **2020**, *38*, 64–72. [CrossRef]